

Spatial Variations in Recent Storm Signals: Combining High Resolution CT-scanning and Laser Diffraction Grain Size Analysis

Cassandra Bejeryd



Department of Geological Sciences
Degree Project in Geochemistry 15 HP
Earth Science Programme 180 HP
Spring Term 2025
Supervisors: Malin Kylander & Ylva Palmgren



Stockholms
universitet

Abstract

This project investigates the spatial variability of storm signals in the form of aeolian sand preserved in peat across a transect in coastal bog Laphroaig, located on Islay, Scotland. Its ombrotrophic nature and geographical position within the North Atlantic storm track makes it a good candidate for storm reconstructions. Five short peat cores were collected extending from the dune system sand source to the location of an earlier paleostorm reconstruction, and analysed using X-ray computed tomography (CT) to create high-resolution records of aeolian sand influx of grains $> 125 \mu\text{m}$. These were compared with conventional methods, mainly laser diffraction (LD) grain size analysis. The application of CT-scanning to storm reconstructions is a relatively new method currently under development. There are many benefits associated with it, but its use also presents emerging methodological challenges. Results reveal a general inland decrease in sand influx and grain coarseness, with notable local variations potentially influenced by variations in local depositional environments and anthropogenic disturbances such as bog drainage. A minimum of two major peaks are identified in each core, generally between 10-23 cm and 25-33 cm depth, in the CT data an attempt to preliminarily correlate these was made. Visual alignment of sand influx peaks suggests correspondence with known regional storm events, although the lack of direct dating introduces uncertainty. The advantages of CT for continuous, non-destructive storm proxy records and the value of spatial context in interpreting peat based paleostorm archives are brought forward in this project.

1. Introduction

Winter storms in the form of extratropical cyclones (ETC) are a natural element of the European climate system, typically characterized by concurrent extremes in wind, precipitation, and temperature. Their impacts are far-reaching, contributing to both human displacement and casualties, infrastructural and societal disruption as well as significant economic losses (Feser et al., 2015). There is an expected increase in monetary losses of 8% for each degree C of temperature increase connected to European wind storms (Ranson et al., 2014), but there are many factors to take into consideration when looking into climate modelling and connecting storm damages to climate change, one of which is the decade-spanning natural variability in storm patterns (Catto et al., 2019). Central to the understanding of midlatitude ETCs is the polar jet stream, a fast, high-altitude westerly wind band which forms where the cold polar air meets warmer air from the subtropics (Feser et al., 2015). This fast-moving wind meanders due to land-sea contrasts, creating large wave patterns called Rossby waves. In these waves, low- and high-pressure systems such as the Icelandic Low and Azores High are formed. Storms usually develop in the low-pressure areas along Rossby waves, where there are sharp differences in temperature and pressure.

Studying the North Atlantic storm track and understanding how it has previously shifted in relation to changes in climate is instrumental for the adapting to and mitigation of the effects of these changes to society moving forward. A shift is expected in both the storm track and storm intensity connected to future climate change. However, there are many uncertainties associated with exactly how storminess will be affected due in part to the many parameters involved in the complex climate system (see: Catto et al., 2019). In particular, we are lacking information on longer multi-decadal to millennial timescales about what climate mechanisms actually control storm track position and storm intensities. One way to gain information on the pre-anthropogenic climate is to use paleoclimate archives.

Ombrotrophic bogs are atmospherically fed, something which makes them well suited to studying atmospheric process. They are also easily dated and fairly widespread. Variations in aeolian sand influx, both volume and maximum grain size, have been increasingly used as indicators of storminess (eg. Björck & Clemmensen, 2004; Jong et al., 2006; Kylander et al., 2020; Orme et al., 2016; Vaasma et al., 2025) as the energy required to mobilize and transport larger grains exceeds that of finer material (Tsoar & Pye, 1987), meaning spikes in relatively coarser sand fractions downwind from a source can serve as proxies for stronger winds and past storm events (Björck & Clemmensen, 2004; Kylander et al., 2020). To date the spatial coverage of such records is however low with perhaps a dozen or so records spread throughout the Wales, Ireland, Scotland, Sweden and Norway (Björck & Clemmensen, 2004; Jong et al., 2006; Kylander et al., 2020, 2023; Nielsen et al., 2016; Orme et al., 2015, 2016; Sjöström et al., 2024). In order to capture the wide spatial scales of the ocean-atmosphere mechanisms potentially involved this spatial coverage must be improved.

While significant research has been conducted on this topic there are still many questions to be answered and a need for more data. In their study on the Outer Hebrides, Orme et al. (2016) recorded not only inter-bog variations in sand contents but also intra-bog variations. Likewise, Kylander et al. (2023) found some mismatches in records from the same bog although slightly different proxies were applied. The reliability of the records could be improved by a greater understanding of the spatial variation in storm signals within a single bog. There are also analytical issues associated with these types of records. Grain size analysis has traditionally relied on methods such as sieving, like in the case of Kylander et al. (2020), or laser diffraction techniques (eg. Sjöström et al., 2024). These methods are valuable, but come with limitations such as the need for time consuming, multistep labour-intensive, destructive subsampling to separate the sand grains from their host matrices as well as the incapacity of producing continuous records. In the case of laser diffraction there has also been some questioning of the reliability of its grain size results (eg. Houghton et al., 2024).

It has previously been shown that X-ray Computed Tomography (CT) scanning can offer a powerful, non-destructive way to detect and analyse grains in different matrices (Cederstrøm et al.,

2021; Houghton et al., 2024; van der Bilt et al., 2021). By passing X-rays through a sample from multiple angles, this technology creates detailed cross-sectional images. These are then reconstructed into a 3D model and materials are detected and distinguished based on their density differences. In the context of storm reconstruction, CT scanning enables the detection of sand grains in peat due to their higher density relative to the matrix, this means sand-rich layers associated with high-energy depositional events may be located. The benefits of this method include a high resolution, non-destructive analysis of grain size distribution in 3D across entire core sections, creating continuous records. Recent works have utilized the same technology to identify barely visible tephra horizons as well as Ice Rafted Debris (IRD) in different matrices, including peat (Cederstrøm et al., 2021; van der Bilt et al., 2021). The application of CT-scanning to storm reconstructions is relatively new and currently under development (Palmgren, unpublished), and while there are many benefits associated with this method, its use also presents emerging methodological challenges. In particular, the high resolution brings with it issues surrounding defined lengths. The large data sets created sometimes require digital segmentation before processing, resulting in a potential for segment boundary artefacts. These challenges can introduce uncertainty into peak detection and grain-size interpretation, aspects which are discussed further in relation to this project's generated data and results.

1.2 Aim

Kylander et al. (2020) established a single long-core peat paleostorm record in the coastal ombrotrophic Laphroaig bog. The island's geographical position directly in the path of the North Atlantic storm track, and Laphroaig's location on the west coast of the island makes it an ideal place to study past storminess (Kylander et al., 2020). The long record was taken approximately 600 m downwind from a beach and dune system. The original sequence was analysed for ash content, environmental geochemistry and grain size using sieving. In this project Laphroaig was revisited almost ten years after the initial coring with the aim of exploring spatial changes in recent storm signals. The specific research objectives were to (i) establish five CT-based continuous grain influx and sand distribution records using a relatively new analytical protocol applied to a transect of peat cores from the Laphroaig bog; (ii) compare these results with conventional laser diffraction grain size and ash content analyses made on the same peat cores; (iii) compare results across the transect of sites and investigate any differences in storm signals moving from the beach inland to the site of the previously published long record (i.e., spatial changes across one of the bogs contributing to the paleostorm record from the source to the sink), (iv) and finally, link the new short records with the long record and, if possible, identify any storm events.

1. Materials and method

2.1 Study site

The Laphroaig bog (55°40006.21"N, 6°14039.22"W) is an ombrotrophic blanket bog located at 13 m a.s.l., near Laggan Bay on the western coast of the island Islay (Figure 1), one of the Inner Hebrides of Scotland (Kylander et al., 2020). The dominant wind direction is W-SW. The surrounding terrain within a 10 km radius is generally flat. After this point there is some elevation to the N-NE. Approximately 600 m from the Laphroaig bog, to the northwest, lies a coastal beach and dune system known as the Big Strand. The bog is dominated by low-growing vegetation with grasses, heather and herbs while the dune system is partially grass covered. The island experiences a mild climate with both evapotranspiration and frost instances being low (Edwards & Berridge, 1994). Between 1991 and 2020, the Met Office (n.d.) reported an average annual precipitation of 1307 mm, the highest volumes of rainfall were recorded in the fall and winter months. Mean temperature and mean wind speed at 10 m were recorded at 12.4 °C (maximum temperature) and 6.4 m s⁻¹, respectively. Below the peatland, the bedrock is composed of low-grade metapelites (Kylander et al., 2020).

Laphroaig has undergone significant anthropogenic alteration in recent years, including drainage and tilling activities. These disturbances took place following the extraction of the 2016 long

core of the Kylander et al. (2020) study. At the time of sampling, the site was noticeably dry, with minimal surface pools and water primarily limited to ditch systems. The bog surface was characterized by sparse, dry vegetation cover.



Figure 1: Maps of the study area. 1A: Map of the geographical location of Islay, Scotland. 1B: Map of Laphroaig bog on the island. Coordinates for this peatland are $55^{\circ}40'06.21''\text{N}$, $6^{\circ}14'039.22''\text{W}$. 1C: Map of the Laphroaig short core transect with coring sites for each core collected as well as the location of the long core collected in 2016 by Kylander et al. (2020). Map source: Google Earth.

2.2 Sampling

In early April 2025 five short cores were collected along an transect extending from the 2016 coring location (Kylander et al., 2020) towards the western edge of the Laphroaig bog and the beach and dune system (Figure 1C). All cores were collected by sawing into the peat either from the surface or, in two cases, from the side of a ditch (Table 1). For the ditch cores, the outermost surface peat was removed prior to sampling to avoid sand having moved in laterally. There were no appropriate locations to sample nearer to the beach and dunes. Sampling was performed by Dr. Malin Kylander.

Table 1 gives an overview of the basic information of each core collected along the transect.

CORE	Sampling surface	Length (cm)	Coordinates
LAPH-1	Ditch	40	55°40'08"N, 6°14'47"W
LAPH-2	Surface	50	55°40'08"N, 6°14'50"W
LAPH-3	Surface	30	55°40'08"N, 6°14'53"W
LAPH-4	Surface	28	55°40'07"N, 6°14'55"W
LAPH-5	Ditch	55	55°40'06"N, 6°15'01"W

The short cores were split into archive and working halves. The latter were measured and then initially subsampled into 2.4 x 2.4 cm plastic U-channels by cutting with a stainless-steel knife and scissors on a plastic cutting board. The lengths of the subsampled cores ranged from 8-25 cm depending on the original core. The U-channels with the sub-cores were sealed at the ends with electric tape and a foam barrier was used, when possible, to separate the ends of the cores from the ends of the U-channels due to the high density of the tape. The sub-cores were then kept in plastic in a cool room (temperature of about 8°C) until the CT scanning was completed.

2.3 CT scanning

The U-channel peat cores and a set of peat grain size standards (see below) were scanned using a Geotek Rotating X-ray CT (RXCT) system at the Department for Geological Sciences, Stockholm University set at the following parameters: a voxel size of 30.05 μm , a voltage of 60 kV, and a current of 500 μA . Instrument configuration settings were applied according to the manufacturer's manual. The scan sequence was optimized to minimize background noise, maximize resolution and reduce file size as much as possible. The application of a physical 0.125 mm copper filter reduced noise and beam hardening artifacts by removing low-energy X-rays prior to imaging (Brooks & Chiro, 1976; Cooper et al., 2007), improving contrast between sand grains and the surrounding peat matrix. The scanning geometry included a distance of 1170 mm between source and sample and a detector distance of 265 mm. A rotational image was produced every 0.4°.

As the purpose of this study was to look at sand grain sizes starting at approximately 125 μm in diameter, a voxel size of 30.05 μm^3 was selected to ensure reliable detection, keeping the voxel size smaller than the smallest feature of interest for the purpose of avoiding partial volume effects (Cederström et al., 2021).

2.3.1 CT calibration using standards

To calibrate the CT-derived sand estimates, a set of physical standards created by Ylva Palmgren were included with each core scan. These standards are synthetic and consist of known quantities of sand grains (125-250 and 125-1000 μm size range) embedded in a peat matrix. The sand content of each standard was quantified independently using a combination of manual grain counts and laser diffraction analysis (Mastersizer 3000, Malvern Instruments), providing a reliable reference for

relative grain size distribution and abundance. The two standards were scanned alongside each peat core using identical CT parameters (voltage, current, voxel size, etc.).

The CT scans were processed in Avizo 3D with the purpose of evaluating which interactive threshold produced the most accurate binary segmentation for each scan based on the standards with a known grain count. This process enabled a scan-specific calibration of CT thresholds, where the chosen settings would best reflect the true grain distribution in each core. Threshold values were iteratively adjusted for each scan based on visual inspection and quantitative comparison to the standards. Specifically, thresholded grain data was exported from Avizo and compared to the Mastersizer-derived sand abundances using a custom Python script (CPY1) developed by Ylva Palmgren. This script produces both grain size distribution histograms to compare CT-detected grains with laser diffraction profiles, and correlation analyses (Pearson's r) between CT-derived sand volumes and known relative sand contents. High correlation coefficients (typically $r = 0.94$) and strong alignment in grain size profiles validated the threshold selection for each scan. A second supporting approach using the grains found via the label analysis were also filtered using the histogram EqDiameter operation, grains smaller than $86.4 \mu\text{m}$, the smallest known grain size previously measured in the standards, were filtered out. The resulting amount (% of grains in core segment larger than $86.4 \mu\text{m}$ multiplied by the number of grains found in the core at each threshold) was then compared to sample data. By combining the results of these two methods a threshold was chosen for each scan. This process enabled a scan-specific calibration of CT thresholds, ensuring that the chosen settings best reflected the true grain distribution in each of the scanned peat cores

2.3.2. CT processing

For the 3D visualization, the material was reconstructed using the Geotek reconstruction software after each CT scan was completed. The center of rotation was manually set to -15° . The cross-sectional images (slices) were visually inspected to find the start and end points of each sub-core. The subsequent processing was then performed in Avizo 3D following the steps laid out in Cederström et al. (2021). The U-channels were cropped to only visualize the peat cores using the volume edit function. Interactive Thresholding was then applied to segment the CT-data and isolate the sand grains based on their greyscale values connected to their density differences, creating a binary image of the sand grains (sand=1, background=0). These binary images did however lack sharp edges, especially at the boundaries of the clasts, due to partial volume effects which blur boundaries and distort segmentation, making accurate analysis difficult without further processing. To overcome this, a prearranged recipe was applied through the operation recipe player in Avizo 3D. This performed the following operations: The module Closing, with its default settings, dilated the grains slightly to fill small gaps and holes and then eroded them back to their original size, only smoother. This restored the boundaries of grains that were distorted by partial volume effects, producing more well-defined grains. The Separate Objects module was applied with default settings to separate adjoined grains and prevent touching grains to be counted as one. By then applying Label Analysis each individual grain within the threshold was identified and given coordinates (BaryCenterX/Y/Z). Diameter and shape were measured via EqDiameter and Shape_Va3D, respectively. The Sieve Analysis module was then applied for digital sieving based on the EqDiameter of the grains to classify particles by size fractions: 125-2000 μm , where the latter was chosen as an arbitrary, large upper limit.

All five peat cores were CT-scanned and processed in Avizo 3D. The entire scanned length was successfully processed for four of them. In the case of LAPH-2.1, however, the data for the full 55 cm core length was not retained, only the upper 39 cm. Although raw scan data for the full length is available, the lowermost part was not included in the processed output. Due to time constraints the data processing could not be repeated and the cause of this data loss remains unclear.

The Label Analysis data was exported from Avizo 3D as CSV files. As the length of the CT scanned cores often exceeded the one recorded during subsampling by a couple of mm, segment lengths were then defined for each core based on their lengths recorded during subsampling and grains outside the defined core boundaries were identified using an excel function. These excess portions were trimmed from the top and bottom of the core to bring the core length in line with the measured segment length from the subsampling. The applied excel-function also served to adjust the raw coordination data, specifically the BaryCenterZ-coordinate of each grain within each core was

adjusted, it recalculated how far into the core segment each sand grain was located based on the newly defined length, but kept the value within the range of 0.1 μm to max defined depth. A custom python script (CPY2) provided by Ylva Palmgren then aligned the core segments based on their depth and filtered out any grains smaller than 125 μm , converted depth from μm to cm and binned grains into 1 cm intervals based on their recalculated BaryCenterZ-coordinates, and counted the number of grains belonging to each 1-cm interval. Sand grains were categorized into three different size classes: 125-250, 250-500 and >500 μm and the script calculated grain counts, grain size distribution (%) and sand influx in grains cm^{-3} .

Due to the high resolution of the scans, the data output of some of the longer and/or more sand rich cores became too much for the computer to process in Avizo 3D. For this reason, sub-cores belonging to LAPH-3.1 and LAPH-5.1 were digitally split into equal halves based on slice number to reduce the load on the computer. Each sub-core was segmented and separately processed, with the boundary between segments defined so that the final slice of one segment was also used as the initial slice of the next, resulting in a one slice overlap. These digitally split segments only had excess grains removed from the inter-segment seam, not the midcore digital seams.

2.4 Grain size: Laser diffraction

2.4.1 Pretreatment

Due to time limitations, the laser diffraction analyses focused on LAPH-5.1, LAPH-3.1 and LAPH-1.1. After CT-scanning, the peat U-channel samples were subsampled at 2 cm intervals and transferred into pre-dried crucibles, which were then placed in a drying oven at 105 $^{\circ}\text{C}$ overnight. After drying, the crucibles were cooled in a desiccator before the dry weight of each sample was recorded. The samples were subsequently combusted in a muffle furnace (Nabertherm P 330) at 500 $^{\circ}\text{C}$ for 4 h (Sjöström et al., 2018), then returned to the desiccator to cool prior to final weighing. Ash content was calculated using the formula: (ash weight/dry weight)* 100.

To remove carbonates and combustion residues which otherwise could interfere with laser diffraction analysis, ashed samples were transferred to 50 mL Falcon centrifuge tubes, to which 5 mL of 10% HCl was added. Samples were vortexed and left to react at room temperature for 2 h (Sjöström et al., 2024). Following acid treatment, tubes were filled with Milli-Q water for rinsing. This was followed by three centrifugation cycles at 4000 rpm for 10 min each (Sjöström et al., 2019). Between cycles, the overlying liquid was carefully removed down to approximately 5 mL using a sipper mechanism to avoid disturbing the sediment. Samples were then vortexed and refilled with fresh Milli-Q water.

Following the acid wash, residual organic matter was indicated by the coloration of several samples and subsequently confirmed by microscopy. As a result, an additional hydrogen peroxide (H_2O_2) chemical oxidation treatment was carried out (Gray et al., 2010; Újvári et al., 2016; Sjöström et al., 2023). To each sample contained in 5 mL of Milli-Q water 5 mL of 30% H_2O_2 was added, resulting in a final concentration of approximately 15% H_2O_2 . The tubes were placed in a water bath maintained at 95 $^{\circ}\text{C}$ for 4 h. To compensate for evaporation during heating, additional 15% H_2O_2 was added as needed. Manual stirring was performed every 20-30 min. The samples were then cooled to room temperature and left to soak in the H_2O_2 over several days. They were then diluted with Milli-Q water and the rinse-and-centrifuge routine from the HCl soak was once again applied.

2.4.2 Instrumental settings

A Malvern Mastersizer 3000 (henceforth MS) equipped with He-Ne red laser with a wavelength of 632.8 nm and a 300 mm lens blue light LED with a 470 nm wavelength was used for grain size analysis. Depending on sample size, either a Hydro LV (600 mL) or Hydro MV (120 mL) wet dispersion unit was connected to the MS. Sodium hexametaphosphate was used as a chemical dispersant at concentrations of 0.5% to disaggregate the grains in each sample (Sjöström et al., 2023). They were each left in this solution for three minutes (at 2120 rpm for MV and 3500 rpm for LV), during which a 60 s ultrasound treatment was performed (at 60% for MV and 80% for LV). An

obscuration range of 2-17% was accepted, but the aim was 5-15% (Huseynova, 2018). If obscuration reached above 17% the sample in question was diluted. The grain size distribution of each sample was measured with five repetitions from which an average for each sample was calculated and then sorted into six grain-size classes (<38, 38–63; 63–125; 125–250; 250–500 and > 500 μm), ratios and cumulative percentages were calculated.

1. Results

It should be noted that the resolution differs between data sets. Raw CT data, originally recorded at μm scale, was binned into 1 cm resolution. Subsequent subsampling of the U-channels was carried out at 2 cm intervals.

3.1 CT Scanning

3.1.1 Sand influx (grains cm^{-3})

From the results of the CT-scanning, a distinct general pattern of sand influx can be observed: all cores displayed at least two main horizons of sand enrichment, usually a smaller at a shallower depth, followed by a larger further down, with the exception being LAPH-1.1 whose main peaks are of similar magnitude. Figure 2 illustrates the aeolian sand influx, i.e. the amount of sand grains $\geq 125 \mu\text{m}$ cm^{-3} in each core along the transect, increasing in distance from the upwind dune system (left to right). Core seams are represented by coloured horizontal lines where the yellow represents the physical break between core segments and the red dashed line represents digital intra-sub-core segmentation for Avizo 3D processing. The shaded red area surrounding the dashed line indicates the maximum potential uncertainty at each digital boundary.

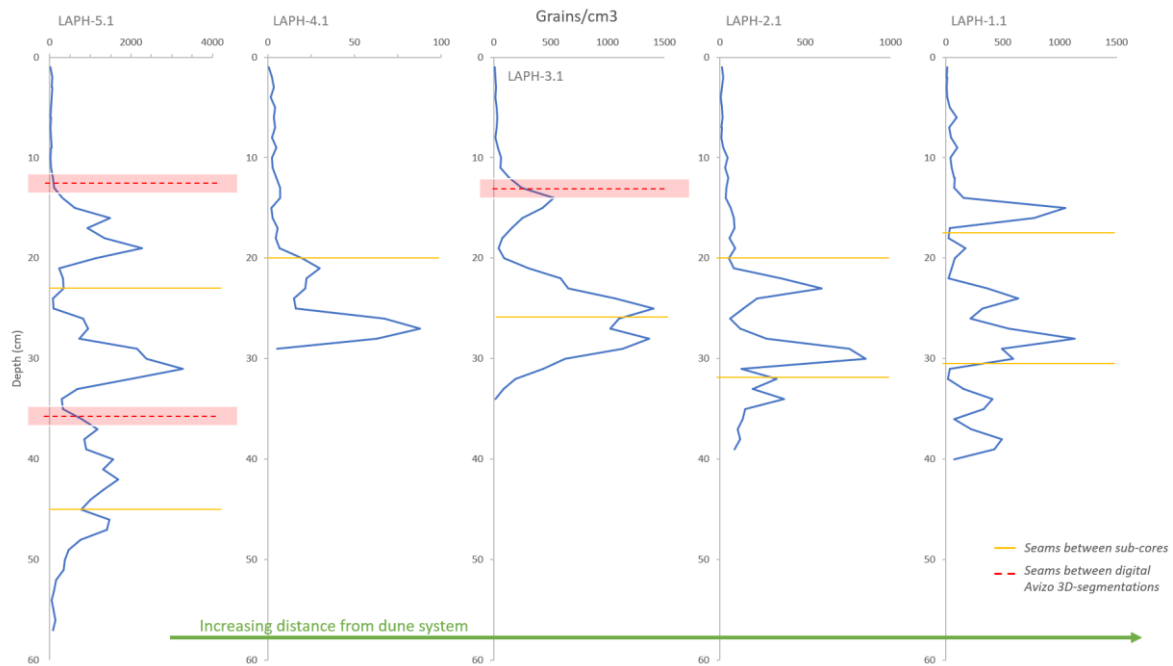


Figure 2: Sand influx (grains cm^{-3}) of the CT-scanned short cores along the Laphroaig bog transect, with distance to main sand source increasing from left to right. Physical and digital core boundaries (seams) are indicated by coloured lines. The shaded red area surrounding the digital seams indicates maximum area of uncertainty, a total of 2 cm due to the 1 cm binning resolution (see Section 2.3).

LAPH-5.1, the core closest to the dune system, exhibits the highest influx of $\geq 125 \mu\text{m}$ sand along the transect with peak concentrations exceeding 3000 grains cm^{-3} (Figure 2). Several horizons of relative sand enrichment can be observed within the core at approximate depths 15-20, 26-33, 36-48 cm. Local peaks are observed at 16, 19, 26-27, 31, 37, 40, 42 and 46-47 cm, most of which reach concentrations

above 1500 grains cm^{-3} . The peaks at 19 and 31 cm are the largest ones with >2000 and >3000 grains cm^{-3} , respectively.

Second closest to the dune system is LAPH-4.1. Here a marked decline in sand input is observed with maximum values below 100 grains cm^{-3} and two clearly defined horizons of increased influx between 20-23 and 25-29 cm depth, with maxima at 21 and 27 cm, respectively. At all other depths the influx remains at levels >10 grains cm^{-3} . Minor variations in peaks can be observed at approximately 3, 5-7, 9, 13-14 and 17 cm depth, all beneath 10 grains cm^{-3} .

Sand enriched horizons in the core LAPH-3.1, taken halfway along the transect, can be observed at approximately 12-17 and 21-32 cm, with concentrations of about 500 and 1400 grains cm^{-3} , respectively, the first peak occurs at 14 cm depth. The second, greater horizon has two individual peaks of similar magnitude at 25 and 28 cm depth, separated by a relative low at 27 cm reaching approximately 1000 grains cm^{-3} . A small increase in sand influx is also observed at 10 cm depth.

As described above, CT data from LAPH-2.1 includes only the upper 39 cm. Two main peaks are registered at 23 (600 grains cm^{-3}) and 29-30 cm (900 grains cm^{-3}) depth. While influx in the upper half of this core remained low in general (>25-100 grains cm^{-3}), some variability can still be observed, like the minor peaks at 2, 6, 10, 12, 16-17 and 19 cm depth. More local peaks are recorded at 32, 34 and 38 cm.

At the distal end of the transect at LAPH-1.1 an increase in sand influx is once again observed. Here, local peaks are recorded at 6, 9, 19, 24, 30, 34-35 and 38-39 cm, with several of these peaks reaching concentrations of approximately 500 grains cm^{-3} . The main peaks are found at 15 and 28 cm, both reaching approximately 1100 grains cm^{-3} .

Worth noting is the highly similar pattern in the sand influx between depths 0-20 in core LAPH-2.1 and 0-18 in core LAPH-4.1. The variation between peak and trough in this interval is small, but between these cores the patterns line up very well, only offset by approximately 1 cm.

3.1.1 Sand size distribution

The five cores sampled along the intra-bog transect reveal a pronounced and generally consistent dominance of the 125–250 μm grain size class (Figure 3). However, individual cores, most notably LAPH-5.1 and LAPH-3.1, exhibit marked increases in coarser fractions at specific depths.

In LAPH-5.1 peaks in the 250-500 μm size fraction exceeding 10% of the cumulative percentage occur at the following approximate depths: 10-11, 15, 17, 19-20 and 30-31 cm. Out of these, the 10, 20 and 30 depth ones coincide with the presence of the >500 μm fraction. It is also found in the less pronounced peaks of the 250-500 μm size fraction at 15-17, 38 and 55 cm depth. In LAPH-4.1 the only peaks of the 250-500 μm size fraction exceeding 10% are found at 2 and 15 cm depth. There are no >500 μm grains present. LAPH-3.1 has a baseline of many minor peaks and troughs in the 250-500 μm size fraction at just below 10% throughout the core with the exception of approximate depth 18-20 cm where the 125-250 μm dominates almost entirely, especially at 18 cm. The other shift in this core occurs at approximately 4-5 cm depth where the 250-500 μm main peak occurs, coinciding with the main peak of the >500 μm size fraction in the core. Two other minor peaks of the coarsest fraction occur at 10 and 18 cm depth. In LAPH-2.1 and LAPH-1.1 there is a fining of the sand and the >500 μm fraction is entirely absent.

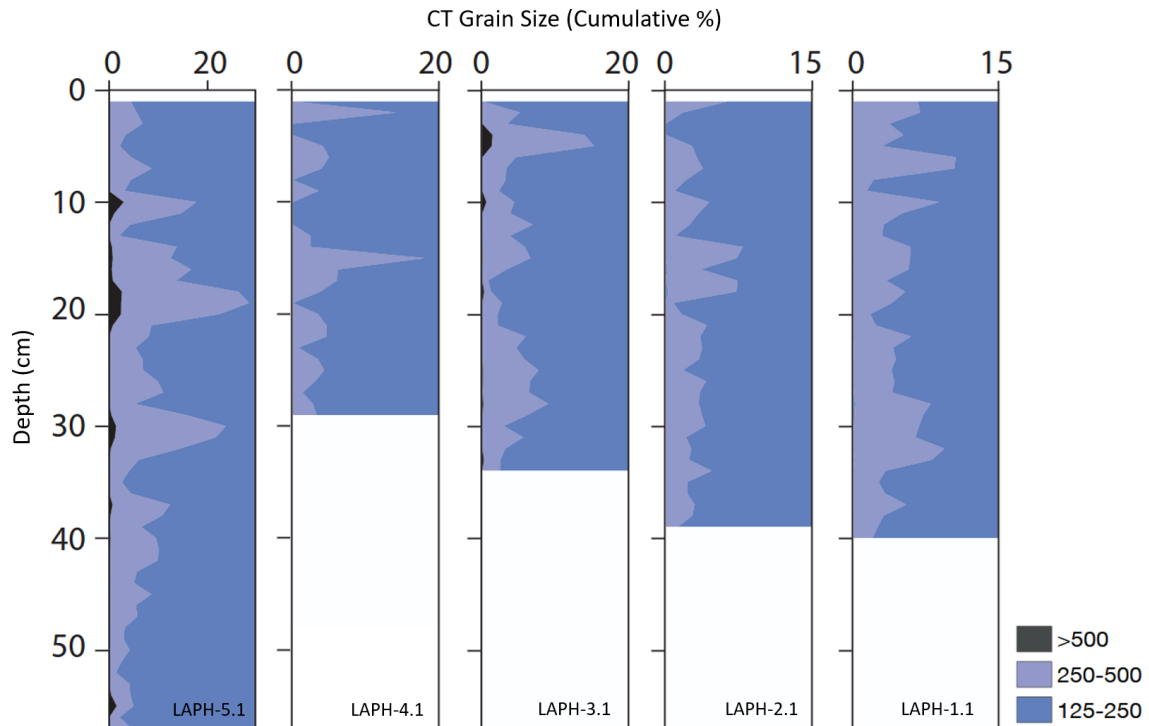


Figure 3 illustrates the grain size distribution data from the CT-scanning of the five short cores along the transect at Laphroaig. Note that the x-axis values are not the same across all graphs, and each display only the upper 15–20% of the cumulative distribution.

3.1.2 Sand size distribution compared with sand influx

A comparison of CT-derived grain size distribution (Figure 3) and sand influx (Figure 2) across the transect reveals some spatial variability. In LAPH-5.1, the core located closest to the dune system, sand influx peaks coincide with a higher proportion of coarse grains (250–500 μm and >500 μm). This coarse grain signal generally weakens inland: mid-transect cores LAPH-3.1 and LAPH-2.1 exhibit reduced sand influx and a noticeable drop in coarse grain occurrences compared to LAPH-5.1. Compared with LAPH-2.1, there is once again a small increase in sand influx for LAPH-1.1. In the second most proximal core, LAPH-4.1, sand influx is minimal and to the greatest extent out of all the cores dominated by fine grains (125–250 μm), even if it has two peaks in the 250–500 μm size fraction exceeding more distal cores in magnitude.

While there are more peaks in grain size than in sand influx, peaks in the latter do generally seem to correlate with peaks in >250 μm fractions, but the magnitudes do not necessarily match. In LAPH-3.1 for example, the greatest peak in the coarser grain size fractions is observed at approximately 4–5 cm depth, a depth which only sees a marginal increase in sand influx, the other place within the core where >500 μm grains show an increase is at 10 cm, once again at a very minor influx peak. Both main peaks in sand influx (25 and 28 cm depth) are associated with an increase in the 250–500 μm fraction.

3.2 Laser diffraction

3.2.1 Full grain size distribution

Laser diffraction (LD) analyses were made at 2 cm resolution for LAPH-5.1, LAPH-3.1 and LAPH-1.1. In figure 4, all measured grain size fractions during LD grain size analysis are presented: Here it is clear that the two dominant grain size fractions are clay (<38 μm) and fine sand (125–250 μm). Silt reaches zero or near zero values in all three cores, but especially LAPH-5.1 and LAPH-3.1. The coarse sand (>500 μm) grain size fraction only appears to be present in cores LAPH-5.1 and LAPH-3.1, and

only just barely at >30 cm depth for the latter. Notwithstanding the gaps in the record, the variability in grain size distribution shows a similar pattern at all three sites.

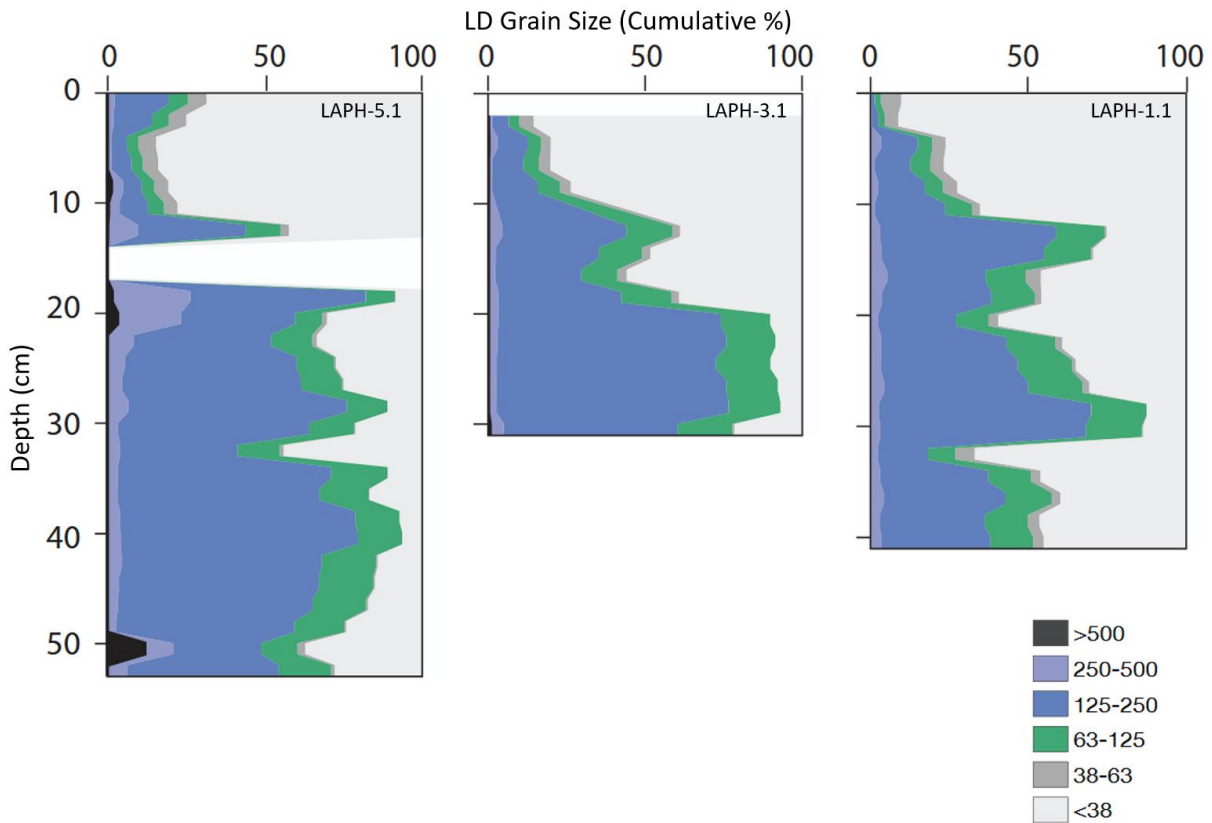


Figure 4 illustrates the results of the LD grain size analysis with all measured size fractions present with larger grain sizes presented on the left.

3.2.2 Cumulative sand fraction >125 µm

For comparison with CT grain size data the focus here is on the >125 µm sand fractions. The cumulative percentage above >125 µm is shown in Figure 5. Between the individual cores a pattern in the peaks and troughs can be observed. For LAPH-5.1 peaks are observed at 12, 18, 28, 34 and 38-40 cm depth. The main peak appears to occur at shallower depths where almost 90% of all grain sizes recorded at this depth belonged to the >125 µm size fraction. Further down the core the baseline seems to be at around 60% sand >125 µm, coupled peaks reaching about 80% and a trough just below 30 cm depth.

There are some inconsistencies in depth and some uncertainties due to data gaps, but despite this, two main peaks can be observed in cores LAPH-3.1 and LAPH-1.1. For LAPH-3.1 they occur at 12, 22-24 and 28-30 cm, although the trough between the latter two is minor enough for the depths between 22-30 cm to be interpreted as a single peak. When looking at the curve for LAPH-1.1, there are peaks at 4, 12-14, 28-30, 36. The horizon of increased sand percentages at the shallower peak occurs at around depth 10-15 cm and the deeper horizon is located at 22-30 cm depth. In LAPH-3.1 the available data registers just over 40% sand >125 µm for the shallower peak and 80% for the deeper. In LAPH-1.1 these values are 60% and 75%, respectively. Common for all three cores are peaks at 12 cm and 28 (in some cases to 30) cm depth (Figure 5).

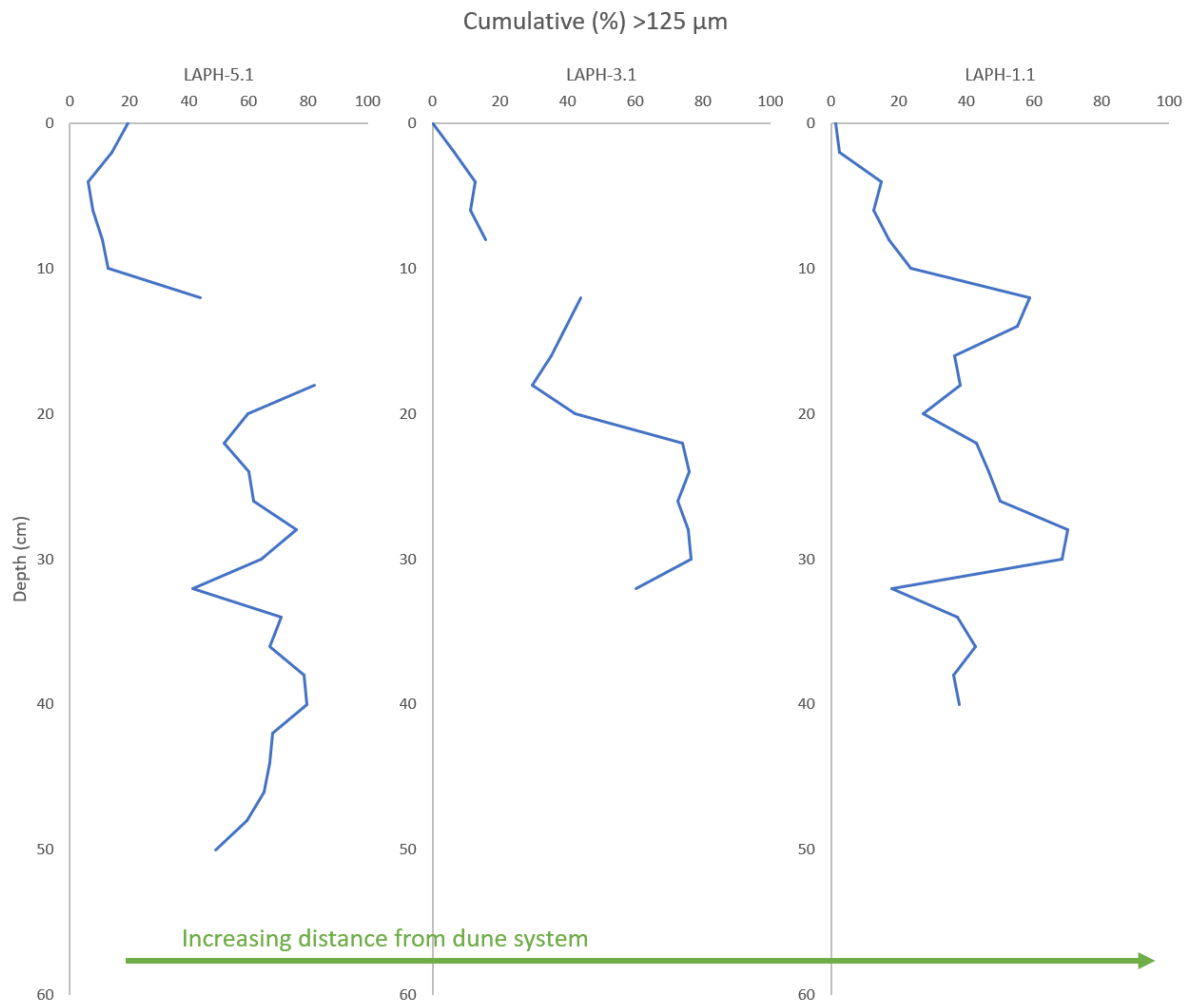


Figure 5: Cumulative percentages of sand grains $>125 \mu\text{m}$ identified through laser diffraction (LD) grain size analysis. While all size fractions: clay ($<38 \mu\text{m}$), silt ($38\text{--}63 \mu\text{m}$), and very fine sand ($63\text{--}125 \mu\text{m}$), were included in the cumulative calculation, only the $>125 \mu\text{m}$ fraction is shown here.

3.2.3 Relative variations in 125-250, 250-500 and $>500 \mu\text{m}$ fractions

When comparing only the $>125 \mu\text{m}$ fractions, grain size distribution shows a dominance of the 125–250 μm fraction in all three cores (Figure 6). LAPH-5.1 has an overall larger portion of the core displaying relatively more of the coarser grain size fractions compared to the other two. Peaks of the 250–500 μm fraction are recorded mainly in the top 10 cm of LAPH-3.1 and LAPH-1.1. Instances of $>500 \mu\text{m}$ increases are few and small overall. In LAPH-5.1 three increases of this size fraction corresponding to 10%, 5% and 25% can be observed at depths 8, 20 and 50 cm, respectively. They are all co-current with increases in the 250–500 μm size fraction. Two small increases are registered in LAPH-3.1 at 4 and 32 cm, again co-current with spikes in the 250–500 μm size fraction. Only size fractions 125–250 μm and 250–500 μm are present in LAPH-1.1.

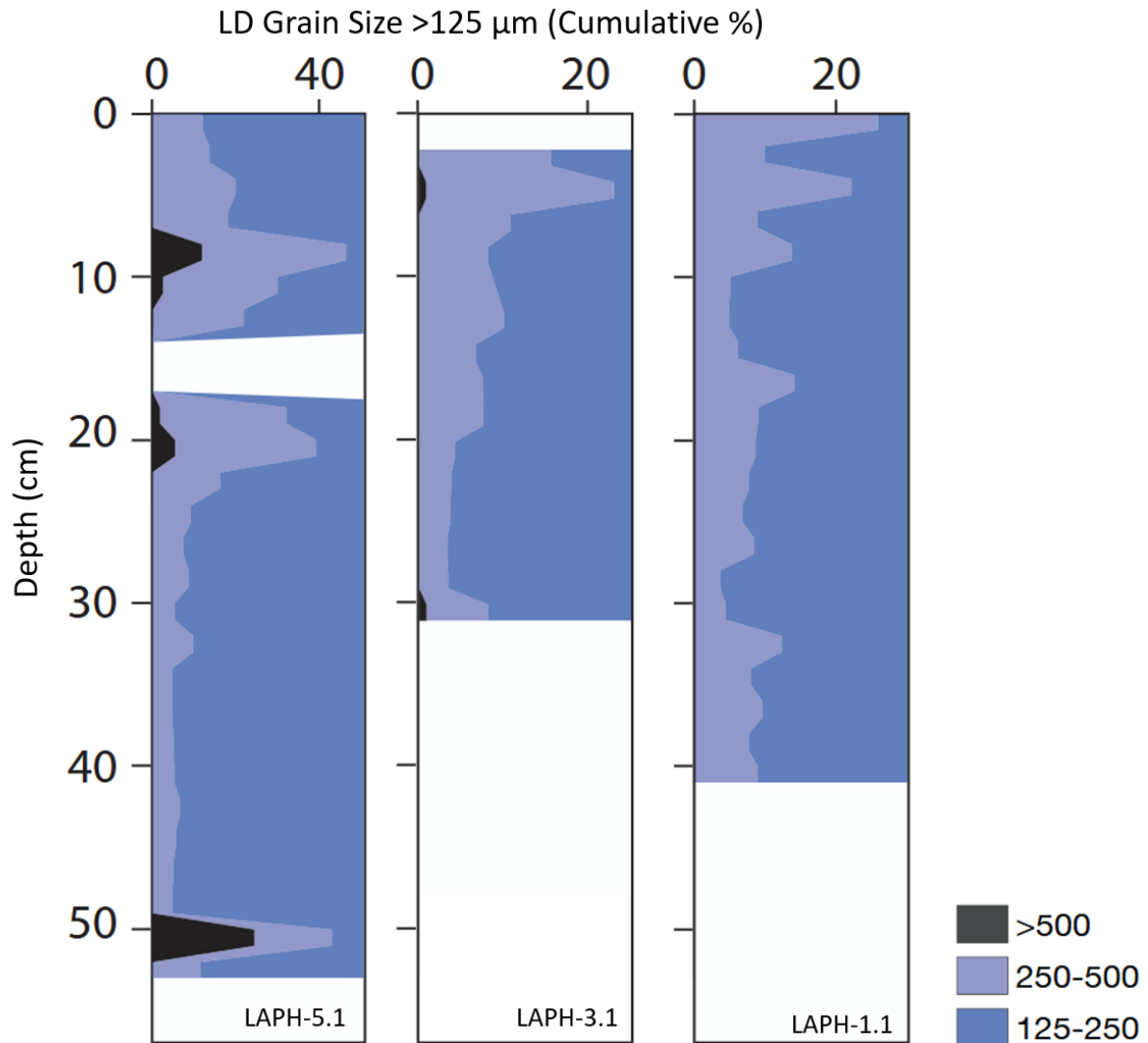


Figure 6 illustrates the recalculated cumulative grain size fractions from the Mastersizer LD grain size analysis, where only grains $>125 \mu\text{m}$ are included. X-axis values are not consistent across all three graphs, only the top 25-40% of the cumulative distribution are illustrated.

3.2.3 Comparison: LD $>125 \mu\text{m}$ grain size and cumulative percentage

In the LD data sets, the sand influx peaks recorded in the cumulative sand percentages (Figure 5) do not consistently align with increases in coarser grain size fractions (Figure 5grain). For example, in LAPH-1.1, the major sand influx peaks (12-14 cm and 28-30 cm depth, as illustrated in Figure 5) correspond to increases in the 125–250 μm size class, while the relative proportions of the 250–500 μm and $>500 \mu\text{m}$ fractions remain low or stable. This pattern is similarly observed across the other cores (see for example depth 22-30 cm for LAPH-3.1 in Figures 5 and 6), where sand influx peaks generally coincide with dominance of the 125–250 μm fraction rather than coarser material. The 12 cm influx peak in LAPH-3.1 on the other hand coincides with an increase in the 250-500 μm size fraction. In the case of LAPH-5.1 there are three peaks of the coarsest fraction ($>500 \mu\text{m}$), at approximately 8, 19-22 and 50-51 cm. Out of these, only the smallest one, at 19-20 cm coincide with an increase in the cumulative sand percentage (Figure 5).

3.3 Ash content

The ash content of the five short cores collected along the intra-bog transect at Laphroaig is illustrated in Figure 7, along with the long core ash content and its ^{14}C age model. Here, a spatial and depth-dependent variation in ash content is shown. Some peaks along the transect are offset from each other by some cm. LAPH-5.1 exhibits the highest ash content overall, with values reaching 50% at 28 cm

depth, displaying five peaks located at approximately 18, 28, 34, 38-40 and 43 cm depth. LAPH-3.1 shows a profile with intermittent peaks reaching just above 30%. LAPH-2.1 and LAPH-1.1 display a continued decrease along the transect, with moderate ash content typically ranging between 10% and 30%, and with the highest values also concentrated below 30 cm depth. In contrast, LAPH-4.1 presents the lowest ash content across the transect, rarely exceeding 6% throughout its entire length. With the exception of outlier core LAPH-4.1 there is a gradual decrease in ash content with increasing distance to sand source.

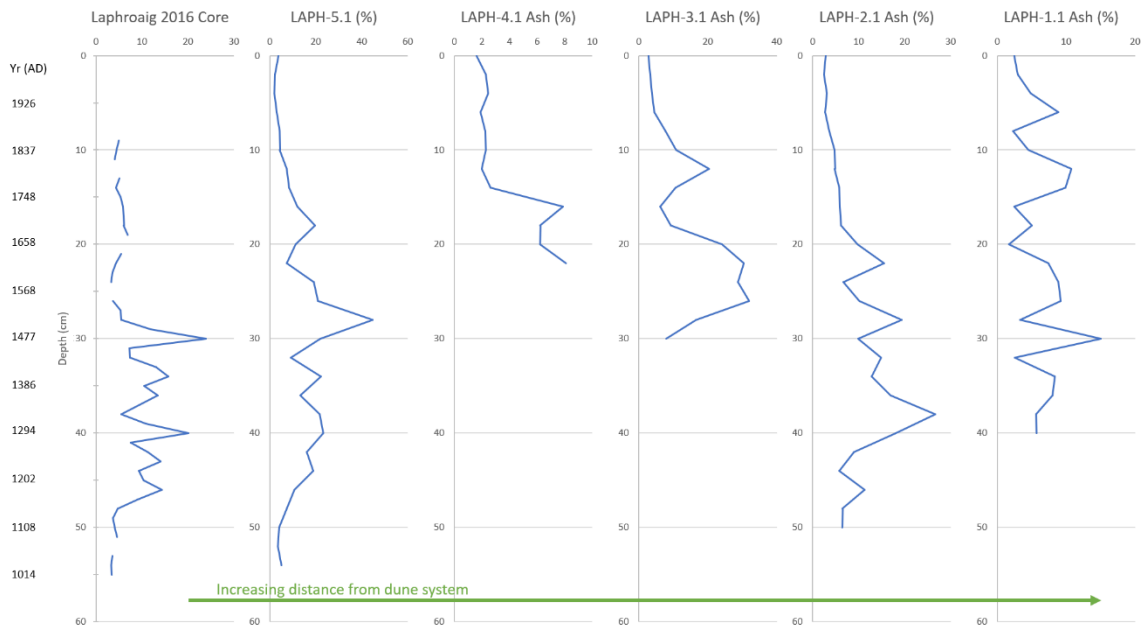


Figure 7: Laphroaig cores along the transect, including the Kylander et al. (2020) long core collected in 2016 (see figure 1C for transect) and their age model presented at a 5 cm interval. Ash content is presented in % and calculated

1. Discussion

4.1 CT data: Analytical considerations

Due to the large file sizes of the CT scans, a total of three core segments from LAPH-5.1 and LAPH-3.1 were digitally split into halves based on slice number prior to processing in Avizo 3D to reduce the computational load (boundaries illustrated in Figure 2). In order to avoid data loss and ensure continuity at the digital boundaries, a single-slice overlap corresponding to the voxel height was included between adjacent halves. This overlap ensured that grains spanning the boundary were not omitted during grain segmentation and analysis, something which was especially relevant considering the difference in voxel size compared to minimum grain size meant larger grains could span multiple slices. This approach did however introduce a potential source of analytical uncertainty which, due to the binning resolution of 1 cm, spans a 1-2 cm range at each digital segment boundary, depending on where within the core it resides. In the cases where grains straddle the boundary between the final slice of one segment and the first slice of the next, they may for example be detected in both halves and counted twice, or be split in such a way that they get misrepresented or fall below 125 μm and get filtered out. Either scenario would, in theory, result in an over- or underrepresentation of the sand influx and grain size data, with the result being artificial peaks or dips in the 1-2 cm surrounding the digital segment boundaries. An alternative approach for dealing with the matter could have been to remove 1 cm at each digital boundary, thus removing the potential for boundary anomalies altogether. This would have ensured that no artificial peaks or dips would have been accidentally interpreted as storm events. The downside of this being the loss of data and gaps in the storminess record.

Upon observing the affected cores and the general trends across the transect however, the transitions around the digital boundaries appear relatively smooth and consistent across the independently processed cores. There are no drastic spikes or drops in sand influx at these depths that would indicate artefacts/anomalies from the slice-overlap. This supports the choice of retaining the full data set without the exclusion of these boundary zones. The upper sand enriched horizon observed in LAPH-3.1 (Figure 2) at approximately 14 cm depth coincides with a digital segment boundary introduced at 12.6 cm during preprocessing. While its proximity to the segmentation boundary introduces uncertainty and, as such, should be acknowledged and interpreted with some degree of caution, the close to identical curve from the ash content supports the interpretation of this peak as a storm event.

Another potential source of uncertainty in the grain size analysis arises from the decision to trim excess data at the top and bottom of each CT-scanned sub-core segment. This trimming was necessary to amend minor inconsistencies between the length of the digital CT core volumes and the segment lengths recorded manually during subsampling. These discrepancies likely stem from differences in resolution as CT data were captured at a very fine spatial resolution (voxel size = $30.05 \mu\text{m}^3$), whereas subsampled lengths were measured with mm to half-cm accuracy. In several cases, the physical cores had uneven or slanted ends, which may have caused sand-bearing material to protrude beyond the manually recorded lengths.

To address this, each core segment was cropped during post Avizo 3D processing by removing an equal portion from both ends based on their individual excess length. This was calculated by the number of slices too many divided by two, bringing the digital data into alignment with the manually measured core lengths. While an alternative approach could have been to keep this excess material and add it on to the ends of the core, this risked introducing artificial layers at the segment boundaries, potentially creating false peaks in the sediment record. Trimming the excess, by contrast, ensured consistency of sand influx across cores but resulted in the loss of some valid data. In some segments, this removed only tens of grains, while in others, such as the LAPH-5.1 and LAPH-2.1 lowermost segment boundaries it amounted to over a thousand each. Consequently, this approach may lead to a slight underrepresentation of sand influx at physical segment boundaries, especially where trimming intersects with layers rich in sand. This may have been significant for the aforementioned cores when considering the placements of said lower segment boundary (Figure 2), one of which (LAPH-2.1) coincides with a smaller peak. However, given the low proportion of affected grains relative to the total dataset and the risk of greater interpretative misrepresentation had the surplus been retained, this method was considered more fitting for the purpose of this project.

A potential limitation of the usage of CT scanning for grain size analysis following the steps laid out in Cederstrøm et al. (2021), that was discovered during this project, was the uncertainty associated with large quantities/concentrations of grains, as were the case of several of the Laphroaig cores. In these cases, a clumping together of the grains could be observed during the Avizo 3D processing and whether or not all of these adjoined grains were properly separated during the application of the Separate Objects module is not entirely certain. This may have resulted in an overestimation of grain size diameter and an underestimation of sand influx.

When comparing the CT-data to the other data sets of this project, no gaps or missed peaks are observed. The non-destructive nature of the method also made it possible to acquire a continuous record of higher resolution with more accuracy than from the more conventional methods. The findings of this project align with recent advances in CT-based sediment analysis, such as those by Cederstrøm et al. (2021) and van der Bilt et al. (2021), which highlight its capacity to non-destructively quantify minerogenic material in high resolution. Although the focus of this project was on storm-derived aeolian sand deposition into ombrotrophic peat bogs rather than marine IRD or tephra-horizons, all three applications benefit from the ability of CT scanning to capture subtle depositional signals reflecting potential events of interest. Like the results of the studies mentioned above, this project underscores the potential for CT data to improve the resolution of paleoenvironmental reconstructions.

4.2 Grain size: CT vs LD

When comparing the overall sand input into the system, represented by sand influx in the CT data (Figure 2) and cumulative sand percentages in the LD data (Figure 5), alongside their respective grain size distributions (Figures 3 and 6), two key patterns emerge. First, both data sets suggest at least two peaks for each core. And second, both methods clearly indicate a dominant 125–250 μm grain size class across all cores, affirming this as the main size fraction associated with sand influx events at Laphroaig. However, a noticeable difference arises in the degree of this dominance. The LD data consistently records a higher proportion of coarser fractions, particularly the 250–500 μm range, and in the case of LAPH-5.1, even a substantial >500 μm component. This key observation is consistent with other studies and is largely attributed to inherent biases in the LD method where a systematic overestimation of grain sizes is reported due to an assumed spherical shape, which leads to an overrepresentation of diameters of elongated, platy or aggregated grains (Konert & Vandenberghe, 1997; Yang et al., 2019). Furthermore, since LD reports grain size by volume percentage, a smaller number of large grains can influence the measurements disproportionately. These factors likely contribute to the elevated coarse fraction signal seen especially in LAPH-5.1, where storm-driven sand influx is presumed to be most intense.

In their comparative study of laboratory techniques for grain size analysis, including LD and X-ray computed tomography (XCT), Houghton et al., (2024) observed a consistent overrepresentation of particles >150 μm in the LD dataset even when including only spherical silica grains in their analysis. Their XCT-derived dataset on the other hand, exhibited the lowest variation in grain sorting among all methods tested. From this it was concluded that XCT was the most accurate technique for capturing grain size distributions in sediments, with the added benefit of XCT uniquely providing access to additional parameters, such as particle shape and orientation. It should be noted that no ultrasonic baths were performed on their samples before measuring, as was done in this project, due to an observed skewing of the results towards finer fractions (Ballard & Beare, 2013, as cited in Houghton et al., 2024).

Another thing worth noting is that in the LD data set the >125 μm cumulative sand percentage peaks do not always align with the observed increases in larger grain size fractions of the >125 μm LD grain size distribution. When looking at the peak at depth 22-30 cm for LAPH-3.1 and 12-14 & 28-30 cm for LAPH-1.1 for example (Figures 5 and 6), the opposite relationship appears to be true. The main peaks in sand percentage, interpreted as sand influx, are here associated with a peak in the 125-250 μm size fraction. Indicating, perhaps, that the dominant size fraction transported over these distances is the smaller one even during these storm events. A case could be made for a lag effect in the transport of the coarser grain sizes to the more distal cores, where coarser particles may have required multiple strong events for transport over this distance. Especially since the most proximal core, LAPH-5.1 displays a closer alignment of the cumulative peaks with the increase in the coarser grain sizes. The increase in the two larger grain size fractions disconnected from the peaks in sand influx could perhaps be attributed to this explanation as well. This does however not account for the lack of sand influx peaks observed at the registered coarser grain depths of the other cores, which would be expected in events high enough in energy for entrainment of coarser grains. Another challenger of this lag interpretation, is the clear alignment between sand influx peaks and coarser grain sizes observed in the CT data. Here, all increases in coarser grain sizes do not correspond to an increase in sand influx, but the increases in sand influx tend to coincide with peaks in the coarser fractions. If LAPH-3.1 is used as an example again, the same lower peak is found in both the CT influx and LD percentage at the same depth (approximately 22-30 cm), but the grain size distribution diverges in trend since the CT data instead suggests an increase of the 250-500 μm for the same section of this core. This contradiction between data sets for the same depth intervals of LAPH-3.1 suggests that one of the methods may be providing a misleading signal and that further investigation into methodological biases and limitations. LD has, as discussed above, been known to overestimate larger grain size fractions in earlier studies (Houghton et al., 2024; Konert & Vandenberghe, 1997; Yang et al., 2019), but in this case it is instead the matter of a potential underestimation. In the discussion of analytical considerations of the CT data (4.1) on the other hand a potential overrepresentation of grain size in sand rich layers due to the clumping together of grains was

addressed. Since this is the largest peak of the core in question, this explanation cannot be ruled out at present.

4.3 Comparative analysis of data and linking it to storminess

The CT scans as well as the cumulative LD results and ash content across the bog transect reveal a general pattern in sand (>125 μm) deposition, albeit with less detail in the case of the ash content and LD due to their lower resolution. This pattern consists of a general reduction in grain abundance and a fining of grains with increasing distance from the dune system, with LAPH-4.1 being the main exception. A minimum of two main peaks in influx are observed in each core, and increases in the coarser grain fractions are associated with these influx peaks in at least the CT data set. This pattern can provide a potential for future interpretation of storm intensity, where only the more intense storm events are likely to have delivered coarse material to cores further inland, whereas even moderate storms might have deposited sand in cores closer to the dune system (Tsoar & Pye, 1987). Due to Laphroaig's geographical position within the North Atlantic storm track, it is especially well suited for this task (Kylander et al., 2020). But in this project the focus will remain on the more fundamental level of storm occurrences, with these alternations between peaks and troughs being interpreted as a variation in atmospheric conditions at the time when each core-level of the peat was exposed at the bog surface and will therefore be used as a proxy for storm-driven aeolian influx (eg. Björck & Clemmensen, 2004; Jong et al., 2006; Kylander et al., 2020; Orme et al., 2016).

A preliminary correlation of the short cores across the transect is attempted by aligning peaks at similar depths of the CT data and comparing sand influx across profiles (Figure 8). Two to three major peaks were identified and tentatively correlated across the transect. The clearest alignment is observed around 27–32 cm depth (purple), where all five cores, including the generally low-influx LAPH-4.1, display coinciding peaks. For the shallower (cyan) and middle (magenta) peaks, alternative alignments are possible at some points, illustrated in the figure by the differently weighted paths. The cyan peak shows the most vertical variability whilst the magenta peak is especially varied in pattern. It also has a larger uncertainty connected to it for cores LAPH-4.1 and LAPH-2.1. These variations across the transect may reflect true variability in how storm events are expressed across Laphroaig. Or they could be representing local differences in depositional environments, or secondary effects as will be discussed further. Future dating of the short cores could further corroborate these preliminary attempts.

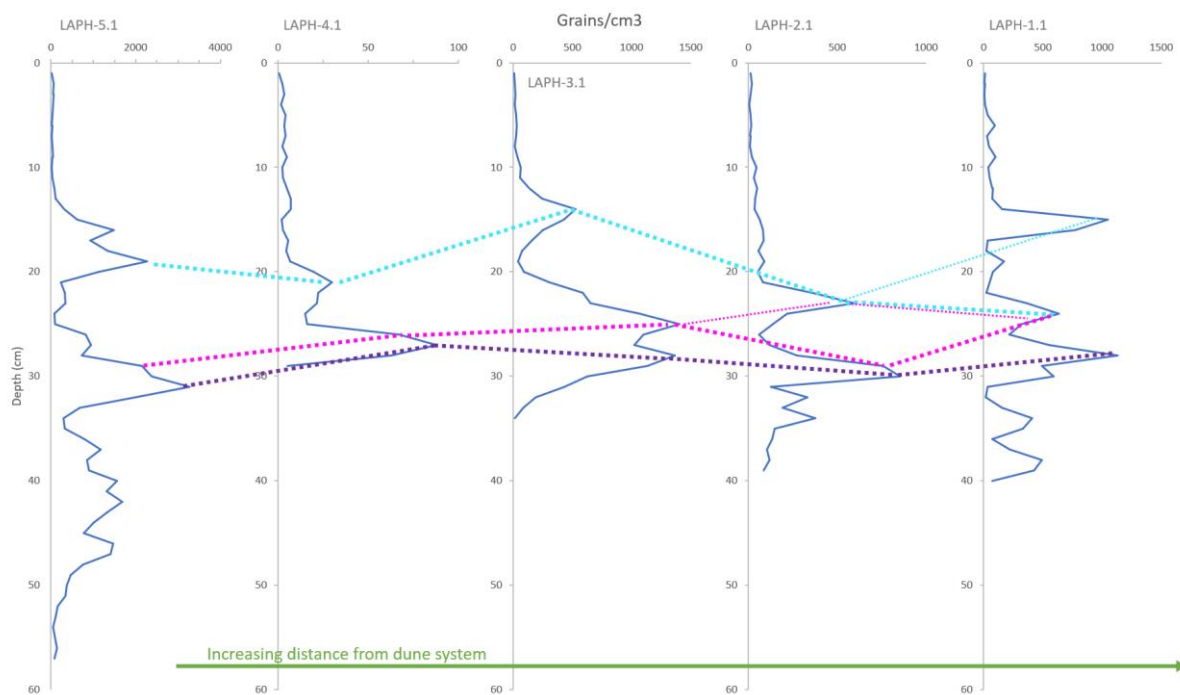


Figure 8 shows the attempt to link CT-scanned cores based on their sand influx. For cores LAPH-2.1 and LAPH-1.1, two alternative scenarios are proposed, indicated by differently weighted lines of the same colours.

There is however, overall, a noticeable variation in the depth at which sand influx peaks – potential storm events – occur between the cores across the transect. In some cases, these differences may to some extent be attributed to recent anthropogenic disturbances which have taken place since the collection of the long core in 2016. Since this initial coring performed by Kylander et al. (2020) at Laphroaig, the bog has undergone tilling and drainage with several ditches having been installed. Due to these disturbances the groundwater level has been lowered, exposing previously water-saturated peat layers to oxygen and creating aerobic conditions that promote microbial activity and more efficient decomposition of organic matter (Holden et al., 2004; Hooijer et al., 2012). This, together with the peat compaction due to decomposition, could have resulted in some level of subsidence of the peat and even compaction of the sand layers within it, thus potentially even overexaggerating the potential signals. The short cores extracted from drainage ditches (LAPH-5.1 and LAPH-1.1) could be more severely affected by these effects due to their increased exposure from multiple faces. Interestingly, they show more peaks compared with the other cores taken from seemingly less disturbed areas of the bog. There is also the matter of minor differences in the individual defined zero depths of each core which could have contributed. Additionally, underlying variability in bedrock topography could contribute to the observed depth variations.

Variations in surface conditions across the bog at the time of storm events may also have influenced the sand retention capacity of individual coring sites. Features such as micro-topography, vegetation cover or surface water (such as puddles) could have acted as traps for deposited sand grains at some locations, preventing their re-entrainment by subsequent winds (Bindler et al., 2004; Tsoar & Pye, 1987). Other locations may have provided conditions favourable for further erosion. Such localized differences in retention potential may help explain the slight, non-gradual variation across the transect in general as well as the markedly lower sand influx recorded in both the CT data and ash content of core LAPH-4.1. Orme et al. (2016) did find a similar trend in intra-bog cores of two peatlands in the Outer Hebrides and attributed it to micro-topography. They concluded the long-term trends observed in sand influx to be replicable and representative of regional storm signal despite this variation.

Another possible actor is spatial variability in peat accumulation rates across the bog. As stated in Belyea & Baird (2006) there is structural heterogeneity in peatlands and areas with slower peat growth would thereby accumulate less vertical depth over the same period, causing sand layers deposited by the same storm event to appear deeper and more concentrated while fast accumulation would lead to the opposite effect. Taken together, these factors provide potential explanations for why a single storm event might be recorded at different depths within the same ombrotrophic bog system. This does however make it more challenging to connect the individual peaks of the different coring sites to each other as well as the long record, which was one of the goals of this project.

Additionally, a slight offset between peak depths within the same core can be observed when comparing data sets, such as the 2 cm discrepancy in LAPH-5 (see LAPH-5 in Figures 2 and 7). This may very well be the result of differences in data resolution and subsampling strategy. While CT data were binned into 1 cm intervals, the subsequent subsampling of the CT-scanned U-channels for the combustion and LD grainsize analysis was performed at 2 cm intervals which may have smoothed or shifted peak positions. Another potential source of discrepancy in core length measurements across datasets arises from the physical subsampling process during the LD pretreatment. Each core was subsampled into cubes approximately 2 cm in length using a knife, which, despite careful measuring and handling, may have introduced small mm-scale inaccuracies at each cut. These seemingly minor errors accumulated over the entire length of a core, slightly altering its total recorded length. This effect is for example noticeable in core LAPH-4.1, where a mismatch in depth between CT-derived (Figure 2) and combustion-derived data (Figure 7) likely reflects these accumulated cutting inaccuracies. Such inconsistencies can shift the apparent position of sand influx or ash content peaks relative to each other, perhaps accounting for part of the shift in depths observed between and in the case of LD and ash contents, within data sets.

4.4 Linking available cores and identifying storm events

Due to gaps in the peat record (Figure 7) of the long core above 30 cm depth (Kylander et al., 2020), meaningful comparisons in this upper section are limited. However, at around 30 cm, a notable correspondence emerges in peak patterns between the long and short cores, with the exception of LAPH-4.1 and LAPH-3.1. Among the short cores, LAPH-1.1, located closest to the 2016 coring site, shows strong alignment: its largest ash peak occurs at 30 cm, matching the long core in depth, though concentration values in LAPH-1.1 are slightly lower. LAPH-5.1 appears to have the ash content profile most similar to that of the long core overall, despite a generally higher sand influx and a 2 cm upward shift, placing its corresponding peak at approximately 28 cm depth. It is possible to transfer the age model from the long core and make a rudimentary dating of the peaks observed in the short cores. From the long core the peak at 30 cm has been ^{14}C dated to 1477 AD (Kylander et al., 2020). If this peak is assumed to be the same as the ones observed at 28 cm in LAPH-5.1 and at 30 cm in LAPH-1.1, then the dating model from the long core may be tentatively applied to shallower sections of the short cores. This provides a preliminary means of identifying potential historical storm events, and linking them to the broader aeolian sand influx storm record developed in recent decades (eg. Björck & Clemmensen, 2004; Jong et al., 2006; Kylander et al., 2020; Orme et al., 2016; Vaasma et al., 2025). For improved reliability of these correlations in a future stage, this report strongly recommends independent dating of the Laphroaig short cores.

In the Laphroaig short cores, the general pattern observed above 35 cm depth from the CT and LD data (Figure 2 and 5, respectively) is at least two main peaks, a smaller one at shallower depths and a larger one deeper down. The exact depth of these peaks varies spatially along the transect, and within data sets, in the former case likely depending on peat decomposition/compaction and the definition of the zero depth at the surface and in the latter perhaps due to resolution differences. If the Laphroaig long core record (Kylander et al., 2020) is aligned with the short cores and the age model from the former transferred to short cores, the larger peak (generally observed at approximately 25–35 cm depth) would be dated to somewhere between 1568 and 1441 AD, depending on the core. Here the long core age model is applied to LAPH-5.1, despite it being the most distal to the site, because of its length and general similarity in profile to the long core. In this case the lower peak dates to approximately 1477–1514 AD and the upper peak to 1658–1676 AD. This is in agreement with the storm events detected in the long core paleorecord, where peaks were observed in 1145–1515 AD and 1675 AD (Kylander et al., 2020).

Based on historical records of coastal storms in Scotland, Hickey, (1997) identifies two distinct periods marked by increased coastal sand movement which are of relevance to the data of this project: 1400–1424 AD and 1625–1699 AD, the latter exhibiting peak activity between 1675 and 1699, at the height of the Little Ice Age (LIA). Nearly a third of the described coastal sand movements occur as a result of gales or storms with predominant north-westerly or western winds, one of the three most severely affected areas were the Outer Hebrides, the island group which lies to the west of the Inner Hebrides, partially sheltering them. Although these time intervals do not perfectly align with the age model used in this study, such discrepancies may be attributed to the inherent limitations of resolution and dating uncertainty (Blaauw, 2010). Nonetheless, the broad correspondence between historical storm records and the observed sand influx signals in this study suggests a potential linkage worth further investigation. Also in general agreement with this is the Halland ombrotrophic bog sediment record (Björck & Clemmensen, 2004) where storm events were observed in 1475 AD and 1650 AD. On the Outer Hebrides Orme et al. (2016) found an inter-bog peak in aeolian sand influx at 1400–1480 AD in their similarly set up study. By displaying similar grain size and sand influx signatures associated with periods of storm events, these support the interpretation of the chosen peaks in the Laphroaig short cores of this project as storm events.

However, in the absence of direct dating of the short cores, connections to the wider established storm record of Northwestern Europe rely primarily on aligning peaks at similar depths and comparing sand influx profiles. While suggestive, this approach carries significant uncertainties and might at the end of the day read more like speculation. Especially given the observed variability in peak depth and magnitude both in this study and in previous work (Bindler et al., 2004; Kylander et al., 2023; Orme et al., 2016).

6. Conclusions

Through this project it can be concluded that varying storm signals can be produced within a single bog. Five short core storm records were established using CT scanning and ash contents. Three of these were analysed by LD for grain size. The resulting data gave indications of possible storm events using the aeolian sand input as a storm proxy. While exceptions existed, the overall pattern observed when looking at and comparing the data sets was a gradual decrease of sand influx as well as a general fining of the grain size along the transect from source to sink. Possible explanations for the variability breaking this general trend have been suggested as follows: small scale variability in micro-topography, vegetation cover, surface puddles and peat accumulation and decomposition rates. These could have influenced the local patterns of aeolian sand deposition.

Despite some encountered limitations, CT scanning has proven a highly useful method for improving the resolution and continuity of paleostorm records, allowing for more detailed insight into storm-related deposition than the more conventional LD, which was hampered by resolution limits and potential grain size overestimation. Despite the lack of direct dating of the short cores, comparisons with the previously dated long core from Laphroaig made estimated age-depth alignments possible through the visual matching of the ash content of core profiles. This made further connections with other paleorecords of the Northwestern Atlantic storm track possible, where a general agreement was observed, providing some support not only for the interpretation of the short core peaks as storm events, but also for the broader regional significance of these inferred storm periods. Due to the lack of direct dating of the short cores, however, the correlations presented in this study remain tentative.

Future work should focus on dating the short cores along the transect and collect elemental data to more clearly link the minerogenic material to its source. This would help build a more complete picture of the conditions at the time of deposition and make stronger connections along the transect as well as to other storm records. With age data, it would also be possible to, with greater certainty, compare the cores to historical storm events, leading to a better understanding of past storm activity and how it relates to past climate patterns and changes in storm tracks to attempt an understanding of future changes and their effects.

Acknowledgements

I would like to express my sincerest gratitude to my supervisors, Malin Kylander and Ylva Palmgren, as well as to Emma Baughman and Carina Johansson, for their expert guidance, encouragement, good humour (dance breaks included), and all the work they have done to help bring this project to fruition. Words aren't enough. Thank you to the IGV Marine Geology group at large for allowing me to use the facilities and for making me feel so welcome. Lee and Rosie—thank you for helping me figure out what matters and what doesn't, without you none of this would have been possible. And Smurf, thank you for being my unwavering companion throughout it all, for keeping my lap warm and my heart full.

Bibliography

Ballard, T., & Beare, S. (2013, June 5). *Particle Size Analysis For Sand Control Applications*. SPE European Formation Damage Conference & Exhibition. <https://doi.org/10.2118/165119-MS>

Belyea, L. R., & Baird, A. J. (2006). Beyond “the limits to peat bog growth”: Cross-scale feedback in peatland development. *Ecological Monographs*, 76(3), 299–322. [https://doi.org/10.1890/0012-9615\(2006\)076\[0299:BTLPB\]2.0.CO;2](https://doi.org/10.1890/0012-9615(2006)076[0299:BTLPB]2.0.CO;2)

Bindler, R., Klarqvist, M., Klaminder, J., & Förster, J. (2004). Does within-bog spatial variability of mercury and lead constrain reconstructions of absolute deposition rates from single peat records? The

- example of Store Mosse, Sweden. *Global Biogeochemical Cycles*, 18(3).
<https://doi.org/10.1029/2004GB002270>
- Björck, S., & Clemmensen, L. B. (2004). Aeolian sediment in raised bog deposits, Halland, SW Sweden: A new proxy record of Holocene winter storminess variation in southern Scandinavia? *The Holocene*, 14(5), 677–688. <https://doi.org/10.1191/0959683604hl746rp>
- Blaauw, M. (2010). Methods and code for ‘classical’ age-modelling of radiocarbon sequences. *Quaternary Geochronology*, 5(5), 512–518. <https://doi.org/10.1016/j.quageo.2010.01.002>
- Brooks, R. A., & Chiro, G. D. (1976). Beam hardening in X-ray reconstructive tomography. *Physics in Medicine & Biology*, 21(3), 390. <https://doi.org/10.1088/0031-9155/21/3/004>
- Catto, J. L., Ackerley, D., Booth, J. F., Champion, A. J., Colle, B. A., Pfahl, S., Pinto, J. G., Quinting, J. F., & Seiler, C. (2019). The Future of Midlatitude Cyclones. *Current Climate Change Reports*, 5(4), 407–420. <https://doi.org/10.1007/s40641-019-00149-4>
- Cederstrøm, J. M., van der Bilt, W. G. M., Støren, E. W. N., & Rutledal, S. (2021). Semi-Automatic Ice-Rafted Debris Quantification With Computed Tomography. *Paleoceanography and Paleoclimatology*, 36(10), e2021PA004293. <https://doi.org/10.1029/2021PA004293>
- Cooper, D., Turinsky, A., Sensen, C., & Hallgrímsson, B. (2007). Effect of Voxel Size on 3D Micro-CT Analysis of Cortical Bone Porosity. *Calcified Tissue International*, 80(3), 211–219. <https://doi.org/10.1007/s00223-005-0274-6>
- Edwards, K. J., & Berridge, J. M. A. (1994). The Late-Quaternary vegetational history of Loch a’Bhogaidh, Rinns of Islay S.S.S.I., Scotland. *New Phytologist*, 128(4), 749–769. <https://doi.org/10.1111/j.1469-8137.1994.tb04038.x>
- Feser, F., Barcikowska, M., Krueger, O., Schenk, F., Weisse, R., & Xia, L. (2015). Storminess over the North Atlantic and northwestern Europe—A review. *Quarterly Journal of the Royal Meteorological Society*, 141(687), 350–382. <https://doi.org/10.1002/qj.2364>
- Gray, A. B., Pasternack, G. B., & Watson, E. B. (2010). Hydrogen peroxide treatment effects on the particle size distribution of alluvial and marsh sediments. *The Holocene*, 20(2), 293–301. <https://doi.org/10.1177/0959683609350390>
- Hickey, K. R. (1997). *Documentary records of coastal storms in Scotland, 1500- 1991 A.D.* (p. 602) [Ph.D. thesis]. <https://ui.adsabs.harvard.edu/abs/1997PhDT.....49H>
- Holden, J., Chapman, P. J., & Labadz, J. C. (2004). Artificial drainage of peatlands: Hydrological and hydrochemical process and wetland restoration. *Progress in Physical Geography: Earth and Environment*, 28(1), 95–123. <https://doi.org/10.1191/0309133304pp403ra>
- Hooijer, A., Page, S., Jauhiainen, J., Lee, W. A., Lu, X. X., Idris, A., & Anshari, G. (2012). Subsidence and carbon loss in drained tropical peatlands. *Biogeosciences*, 9(3), 1053–1071. <https://doi.org/10.5194/bg-9-1053-2012>
- Houghton, J. E., Behnsen, J., Duller, R. A., Nichols, T. E., & Worden, R. H. (2024). Particle size analysis: A comparison of laboratory-based techniques and their application to geoscience. *Sedimentary Geology*, 464, 106607. <https://doi.org/10.1016/j.sedgeo.2024.106607>
- Huseynova, S. (2018). *Determination of particle size distributions of industrial side streams by using laser diffraction and sieving methods.* <https://lutpub.lut.fi/handle/10024/158522>

- Jong, R. de, Björck, S., Björkman, L., & Clemmensen, L. B. (2006). Storminess variation during the last 6500 years as reconstructed from an ombrotrophic peat bog in Halland, southwest Sweden. *Journal of Quaternary Science*, 21(8), 905–919. <https://doi.org/10.1002/jqs.1011>
- Konert, M., & Vandenberghe, J. (1997). Comparison of laser grain size analysis with pipette and sieve analysis: A solution for the underestimation of the clay fraction. *Sedimentology*, 44(3), 523–535. <https://doi.org/10.1046/j.1365-3091.1997.d01-38.x>
- Kylander, M. E., Martínez-Cortizas, A., Sjöström, J. K., Gåling, J., Gyllencreutz, R., Bindler, R., Alexanderson, H., Schenk, F., Reinardy, B. T. I., Chandler, B. M. P., & Gallagher, K. (2023). Storm chasing: Tracking Holocene storminess in southern Sweden using mineral proxies from inland and coastal peat bogs. *Quaternary Science Reviews*, 299, 107854. <https://doi.org/10.1016/j.quascirev.2022.107854>
- Kylander, M. E., Söderlindh, J., Schenk, F., Gyllencreutz, R., Rydberg, J., Bindler, R., Martínez Cortizas, A., & Skelton, A. (2020). It's in your glass: A history of sea level and storminess from the Laphroaig bog, Islay (southwestern Scotland). *Boreas*, 49(1), 152–167. <https://doi.org/10.1111/bor.12409>
- Met Office. (n.d.). *Islay Airport (Argyll and Bute) Location-specific long-term averages*. Met Office. Retrieved 25 May 2025, from <https://www.metoffice.gov.uk/research/climate/maps-and-data/location-specific-long-term-averages/gcgsc8kt2>
- Nielsen, P. R., Dahl, S. O., Jansen, H. L., & Støren, E. N. (2016). Holocene aeolian sedimentation and episodic mass-wasting events recorded in lacustrine sediments on Langøya in Vesterålen, northern Norway. *Quaternary Science Reviews*, 148, 146–162. <https://doi.org/10.1016/j.quascirev.2016.07.011>
- Orme, L. C., Davies, S. J., & Duller, G. a. T. (2015). Reconstructed centennial variability of Late Holocene storminess from Cors Fochno, Wales, UK. *Journal of Quaternary Science*, 30(5), 478–488. <https://doi.org/10.1002/jqs.2792>
- Orme, L. C., Reinhardt, L., Jones, R. T., Charman, D. J., Barkwith, A., & Ellis, M. A. (2016). Aeolian sediment reconstructions from the Scottish Outer Hebrides: Late Holocene storminess and the role of the North Atlantic Oscillation. *Quaternary Science Reviews*, 132, 15–25. <https://doi.org/10.1016/j.quascirev.2015.10.045>
- Ranson, M., Kousky, C., Ruth, M., Jantarasami, L., Crimmins, A., & Tarquinio, L. (2014). Tropical and extratropical cyclone damages under climate change. *Climatic Change*, 127(2), 227–241.
- Sjöström, J. (2018). *Reconstruction of Holocene atmospheric mineral dust deposition from raised peat bogs in south-central Sweden*. <https://urn.kb.se/resolve?urn=urn:nbn:se:su:diva-153723>
- Sjöström, J. K., Bindler, R., Granberg, T., & Kylander, M. E. (2019). Procedure for Organic Matter Removal from Peat Samples for XRD Mineral Analysis. *Wetlands*, 39(3), 473–481. <https://doi.org/10.1007/s13157-018-1093-7>
- Sjöström, J. K., Gyllencreutz, R., Martínez Cortizas, A., Nylund, A., Piilo, S. R., Schenk, F., McKeown, M., Ryberg, E. E., & Kylander, M. E. (2024). Holocene storminess dynamics in northwestern Ireland: Shifts in storm duration and frequency between the mid- and late Holocene. *Quaternary Science Reviews*, 337, 108803. <https://doi.org/10.1016/j.quascirev.2024.108803>
- Sjöström, J. K., Martínez Cortizas, A., Nylund, A., Hardman, A., Kaal, J., Smittenberg, R. H., Risberg, J., Schillereff, D., & Norström, E. (2023). Complex evolution of Holocene hydroclimate, fire and vegetation revealed by molecular, minerogenic and biogenic proxies, Marais Geluk wetland, eastern Free State, South Africa. *Quaternary Science Reviews*, 314, 108216. <https://doi.org/10.1016/j.quascirev.2023.108216>

- Tsoar, H., & Pye, K. (1987). Dust transport and the question of desert loess formation. *Sedimentology*, 34(1), 139–153. <https://doi.org/10.1111/j.1365-3091.1987.tb00566.x>
- Újvári, G., Kok, J. F., Varga, G., & Kovács, J. (2016). The physics of wind-blown loess: Implications for grain size proxy interpretations in Quaternary paleoclimate studies. *Earth-Science Reviews*, 154, 247–278. <https://doi.org/10.1016/j.earscirev.2016.01.006>
- Vaasma, T., Vandel, E., Sugita, S., Tõnisson, H., Suursaar, Ü., Kont, A., & Vilumaa, K. (2025). Storminess reconstruction in the northeastern Baltic Sea region over the past 7600 years based on aeolian sand influx into coastal bogs. *The Holocene*, 35(1), 61–74. <https://doi.org/10.1177/09596836241285783>
- van der Bilt, W. G. M., Cederström, J. M., Støren, E. W. N., Berben, S. M. P., & Rutledal, S. (2021). Rapid Tephra Identification in Geological Archives With Computed Tomography: Experimental Results and Natural Applications. *Frontiers in Earth Science*, 8. <https://doi.org/10.3389/feart.2020.622386>
- Yang, Y., Wang, L., Wendroth, O., Liu, B., Cheng, C., Huang, T., & Shi, Y. (2019). Is the Laser Diffraction Method Reliable for Soil Particle Size Distribution Analysis? *Soil Science Society of America Journal*, 83(2), 276–287. <https://doi.org/10.2136/sssaj2018.07.0252>

Stockholms universitet/Stockholm University
SE-106 91 Stockholm
Phone: 08 – 16 20 00
www.su.se



**Stockholms
universitet**